metals

MDPI

Article

The Dependence of Electrochemical Behavior and Discharge Performance on the Zn/Gd Ratio of Mg-Li-Zn-Gd Anodes for Mg-Air Batteries

Siqi Yin [1,2], Ningyuan Wang [1], Haoxuan Han [1], Zichen Liu [1], Guangzong Zhang [2,3,*] and Renguo Guan [2,3]

[1] School of Mechanical Engineering, Dalian Jiaotong University, Dalian 116028, China; sqyin@djtu.edu.cn (S.Y.); wnyqd2474@163.com (N.W.); jsmh0406@163.com (H.H.); backingzc@163.com (Z.L.)
[2] Key Laboratory of Near-Net Forming of Light Metals of Liaoning Province, Dalian Jiaotong University, Dalian 116028, China; guanrenguo@sina.cn
[3] Engineering Research Center of Continuous Extrusion, Ministry of Education, Dalian Jiaotong University, Dalian 116028, China
* Correspondence: gzzhang@djtu.edu.cn

Abstract: In this study, the electrochemical performance and discharge behavior of Mg-Li-Zn-Gd alloys with α-Mg and β-Li-based anode material are investigated, with the aim to improve the anode performance of Mg-air batteries. The experimental anode alloys with detailed Mg-8Li-xZn-yGd (x = 1, 2, 3; y = 1, 2, 3 wt.%) components are prepared, and extrusion deformation is carried out on these alloys. Simultaneously, scanning electron microscope (SEM), X-ray diffractometer (XRD), electrochemical workstation, and constant current discharge systems are applied for microstructure characterization, corrosion, and discharge performance testing. The results show that the experimental alloys are composed of an α-Mg and β-Li dual matrix, with W-$Mg_3Gd_2Zn_3$, Mg_3Gd, and MgLiZn second phases. Meanwhile, extrusion deformation promotes the recrystallization process through the particle-induced nucleation mechanism. The corrosion resistance is improved with the increasing Zn/Gd ratio, and the extruded Mg-8Li-2Zn-1Gd (LZG821) alloy exhibits the optimum corrosion resistance, with a corrosion rate of 0.493 mm·year^{-1}. In addition, the extruded Mg-8Li-1Zn-1Gd (LZG811) alloy has the optimal discharge performance, with a discharge specific capacity of 1371.04 mA·g^{-1} at a current density of 40 mA·cm^{-2}, and its anode efficiency reaches nearly 70%. The poorer discharge properties of the Mg-8Li-2Zn-1Gd (LZG821) and Mg-8Li-2Zn-3Gd (LZG823) alloys are attributed to their refined grains, which could bring severe intergranular corrosion while increasing the grain boundary density.

Keywords: Mg-Li-Zn-Gd anode alloy; Mg-air battery; extrusion deformation; corrosion behavior; discharge performance

Citation: Yin, S.; Wang, N.; Han, H.; Liu, Z.; Zhang, G.; Guan, R. The Dependence of Electrochemical Behavior and Discharge Performance on the Zn/Gd Ratio of Mg-Li-Zn-Gd Anodes for Mg-Air Batteries. *Metals* **2024**, *14*, 1202. https://doi.org/10.3390/met14111202

Academic Editor: Branimir N. Grgur

Received: 19 September 2024
Revised: 15 October 2024
Accepted: 15 October 2024
Published: 22 October 2024

1. Introduction

Increased energy demand and the emphasis on environmental protection have made important contributions to the development of sustainable energy. Renewable energy sources are usually affected by intermittence and instability, and their promotion is limited. Chemical energy has become a research hotspot with its efficient energy storage and conversion technology, among which battery systems have attracted much attention [1–3]. Battery systems have superiorities such as a long service life, low cost, high specific energy and specific power, etc. [4]. Since the 1990s, many battery systems have been produced, and Li-ion batteries have become mainstream in the market due to their high specific capacity and long service life [5]. However, the energy density of Li-ion batteries is only 100~200 Wh·kg^{-1}. Meanwhile, Li-ion batteries employ flammable liquid electrolytes which pose serious safety risks. Traditional lithium-ion batteries are also limited by high manufacturing costs, and their development is close to the theoretical upper limit, so there is a great need to establish a novel energy storage system [1,6].

Metal–air batteries exhibit a much higher theoretical specific capacity than conventional Li-ion batteries, which is attributed to their unique semi-open structure. Table 1 shows the parameters of various metal–air batteries. Among them, Zn-air batteries are suitable for aqueous systems due to their advantages of low cost, stable discharge voltage, and superior corrosion resistance, but the low energy density and low discharge specific capacity of zinc-air batteries limit their wide application [7,8]. Al-air batteries also show a good theoretical discharge performance, but the dense oxide film on the Al alloy's anode surface and its extremely high self-corrosion efficiency greatly reduce its anode efficiency [1]. Mg-air batteries work well in the fields of armament energy, aerospace, and 3C area because of their relatively balanced high theoretical specific capacity, high energy density, and simple structure [9].

Table 1. Parameters of various metal batteries.

Battery Systems	Voltage (V)	Theoretical Energy Density ($mWh \cdot g^{-1}$)	Theoretical Specific Capacity ($mAh \cdot g^{-1}$)
Li-air	2.91	13,300	3884
Na-air	2.33	2715	1165
Zn-air	1.65	1080	825
Al-air	2.71	8070	2978
Mg-air	3.10	6800	2233

Mg-Li-based alloys are the lightest structural metallic materials, with densities of about 1.25–1.65 g/cm^3, which is lower than pure Mg (1.73 g/cm^3) and magnesium alloys (>1.8 g/cm^3) [10]. Furthermore, the Li element could greatly improve the plastic deformation ability of Mg [11]. When the Li addition is 0~5.7 wt.%, the matrix is a single hexagonal α-Mg matrix. When the Li addition is 5.7~10.3 wt.%, the matrix is changed to a mixed hcp (hexagonal close-packed) α-phase and a bcc (body-centered cubic) β-phase, and the alloy has good strength and plasticity. When the Li content is greater than 10.3 wt.%, only a single β-phase exists, the alloy density is lower, and the strength is worse [12–17]. The addition of Zn components to Mg alloys can cause strengthening of the solid solution and the second phase, and can affect the grain boundary density and grain texture; as such, the Mg-Al-Zn, Mg-Zn-RE (rare earth elements) series is often used [18–20]. Gong et al. [21] reported that Mg-Zn-Ca alloys with moderate Zn addition generated a heterogeneous distributed second phase, which grew along the grain boundaries, and this structure hindered continuous corrosion and enhanced alloy corrosion resistance. However, the addition of too much Zn would decrease the anticorrosion. The addition of RE elements, such as Y and Gd, to Mg-Li-Zn alloys can generate a Mg-Zn-RE ternary phase, which dramatically improves the mechanical properties of the alloys [22–25].

At present, studies on the corrosion and discharge behavior of Mg alloy anodes are rare. Based on the current background, the development of Mg alloy anode materials' discharge properties is of great significance. Sivashanmuga et al. [26] compared the anode efficiencies of Mg-Li alloys in different electrolytes, and found that the anode efficiencies were higher in $Mg(ClO_4)_2$. Liu et al. [27] compared the discharge properties of AZ31, LAZ831, and LAZ1131 alloys, and they found that the addition of Li substantially increased the maximum discharge capacity and anode efficiency, and noted that the activity of Mg-Li alloys is in connection with the delaminated particle-like β-Li phase.

Moreover, the electrolyte of a Mg-air battery is also crucial for improving its discharge performance, and several studies have investigated the influence of the electrolyte on the Mg alloy anode's dissolution reaction. The properties of being innocuous and un-poisonous, being free of contamination, having a low cost, and being suitable for cool environments should be considered. Based on the above reasons, 3.5 wt.% NaCl solution is a frequently used electrolyte in Mg-air batteries, and this work primarily focuses on the Mg alloy anode material composition based on the specified electrolyte.

Given the above, the inferior corrosion of Mg-Li alloys drastically reduces their continuous discharge capability, so some Zn and Gd elements are considered for addition in Mg-Li alloys due to their special atomic structure. Based on the studies of Mg-Zn-Gd and Mg-Li alloy anode materials, this work considers introducing Zn and Gd into the alloy matrix for research, which is a piece of original research. Therefore, this study involves adding Zn and Gd elements to a duplex Mg-8Li alloy containing α-Mg and β-Li to improve its corrosion and discharge performance. The preparation method for the experimental Mg-8Li-xZn-yGd (x = 1, 2, 3; y = 1, 2, 3 wt.%) alloys includes adjusting their Zn/Gd ratio, as well as their Zn and Gd additions; the as-cast alloys are hot-extruded to promote the comprehensive performance of the Mg alloys. The microstructure, corrosion properties, and discharge performance of the extruded alloys are investigated, and the influence of the Zn/Gd ratio on the discharge performance is discussed. This research could give further instructions on Mg-Li-based anodic electrode material design for high-performing Mg-air batteries.

2. Materials and Methods

Five different alloy compositions were prepared by adjusting the Zn/Gd ratio and the Zn and Gd additions, namely Mg-8Li-1Zn-1Gd (LZG811), Mg-8Li-2Zn-2Gd (LZG822), Mg-8Li-3Zn-3Gd (LZG833), Mg-8Li-2Zn-1Gd (LZG821), and Mg-8Li-2Zn-3Gd (LZG823). The experimental alloys were manufactured using high-purity Mg (99.99 wt.%), pure Zn (99.9 wt.%), Mg-10Li, and Mg-30Gd master alloys as raw materials.

The raw materials were dried for 2 h before melting, and then all the raw materials were put into the steel crucible of a vacuum melting furnace for melting. After 20 min of stirring, the alloy melt was breathed into a φ 60 mm mild steel mold. A mixture of SF_6 and CO_2 protection gas was passed through during the casting process. Table 2 shows the practical compositions of the experimental alloys obtained through chemical analysis (inductively coupled plasma mass spectrometry). After vacuum melting, the cast ingot billet was cut into a φ 47 mm × 100 mm bar, and then it was placed inside a thermal treatment furnace at 400 °C × 2 h. Subsequently, the ingot was extruded into a φ 12 mm rod at a 300 °C extrusion temperature and a 1 mm/s extrusion speed under a 15:1 extrusion ratio.

Table 2. Chemical compositions of Mg-8Li-xZn-yGd alloys.

Alloy Composition	Alloy Number	Actual Element Content (wt.%)			
		Mg	Li	Zn	Gd
Mg-8Li-1Zn-1Gd	LZG811	Bal.	8.13	1.04	0.98
Mg-8Li-2Zn-2Gd	LZG822	Bal.	7.91	1.91	2.06
Mg-8Li-3Zn-3Gd	LZG833	Bal.	7.88	3.08	3.11
Mg-8Li-2Zn-1Gd	LZG821	Bal.	8.25	2.10	1.03
Mg-8Li-2Zn-3Gd	LZG823	Bal.	8.04	1.93	2.93

The extruded Mg-8Li-xZn-yGd alloys were investigated by optical microscopy (OM, Leica DMi8 A, Wetzlar, Germany) and scanning electron microscopy (SEM, Zeiss SUPRA 55, Oberkochen, Germany). The SEM was equipped with an energy-dispersive X-ray spectrometer (EDS) detector. The OM and SEM samples were prepared according to standard metallographic sample preparation procedures. The etching solution for the extruded specimens was a mixture of 3 g picric acid, 2.5 mL glacial acetic acid, 50 mL alcohol, and 5 mL deionized water, and the etching time was about 8 s. The secondary phase analysis was carried out by a multifunctional X-ray diffractometer (XRD, Panalytical Empyrean, Almelo, The Netherlands), and the corresponding PDF2-2004 phase database was the referred handbook reference.

A weight loss experiment was conducted for corrosion property measurement. The cubic extruded specimens, measuring 10 × 10 × 10 mm^3, were immersed in 3.5 wt.% NaCl solution for 24 h, after which the samples were taken out and cleaned with 20 $g{\cdot}mL^{-1}$ chromic acid solution to clean the corrosion products, then the mass loss was measured.

The NaCl solution was renewed every 6 h to ensure concentration. The weightless corrosion rate was calculated on the basis of Equation (1) [28]:

$$P_w = \frac{8.76 \times 10^4 \times \Delta g}{A \times t \times \rho} \quad (1)$$

where P_W is the corrosion rate calculated by the weight loss method (mm·year^{-1}); Δg is the mass loss before and after corrosion (g); A is the total surface area of the immersed specimen (cm^2); t is the immersion time (h); and ρ is the density of the specimen (g·cm^{-3}) which was measured by the Archimedes drainage method.

The electrochemical experiments mainly included open circuit potential (OCP), potential dynamic polarization curve (PDP), and electrochemical impedance spectroscopy (EIS) tests. The experimental equipment used was the Wuhan CORRTEST 350M (Wuhan, China) electrochemical workstation with a conventional three-electrode system, and the experimental facility is shown in Figure 1a. The working electrodes (WEs) were the extruded samples, which were derived from the cross section of the extrusion bars, and the working area was 1 cm^2; a saturated calomel electrode (SCE) was regarded as reference electrode; and a 10 × 10 mm platinum plate served as the counter electrode (CE). The OCP test was performed first, with a total measurement time of 1800 s to achieve a relatively stable state. Subsequently, the EIS was carried out, in which the scanning frequency range was 100 kHz~0.01 Hz, and the amplitude of the perturbation signal was 5 mV. Finally, the PDP experiment was carried out at a scanning rate of 1 mV s^{-1}, with a potential range from −2.0 V to −1.4 V. The cathodic branch of the obtained polarization curves was used to obtain the values of the self-corrosion current density I_{corr} and the self-corrosion potential E_{corr}, according to the Tafel cathode extrapolation method, and the average corrosion rate of the experiment alloy can be found using Equation (2) [28]:

$$P_i = 22.85 \times I_{corr} \quad (2)$$

where P_i is the electrochemical corrosion rate (mm·year^{-1}) and I_{corr} is the polarization curve self-corrosion current density (mA·cm^{-2}).

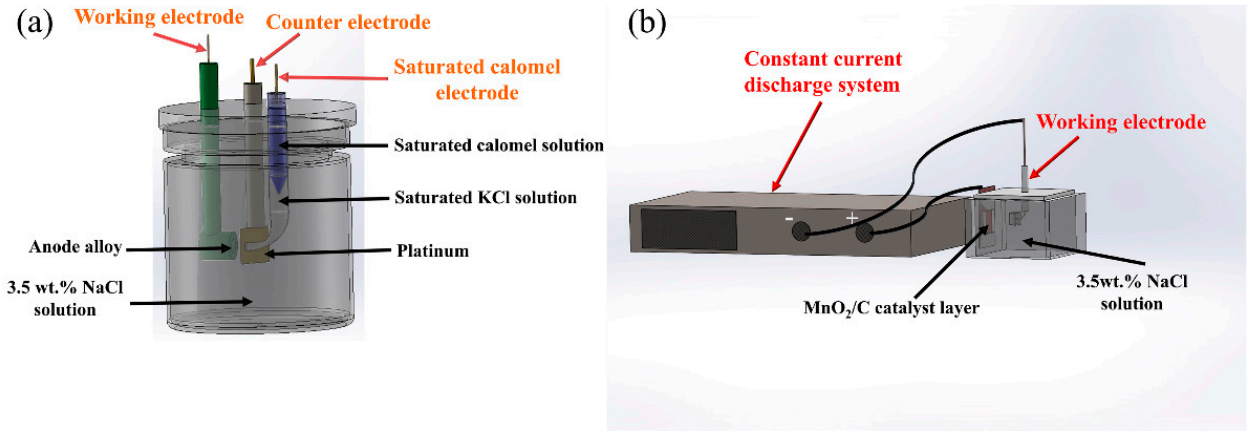

Figure 1. Electrochemical and discharge experimental device diagrams: (**a**) electrochemical experimental device diagram (three-electrode system); (**b**) constant current discharge test workstation.

The LANHE multi-channel Mg-air battery testing system was used to measure the discharge performance of experimental MgLi-Zn-Gd anode materials, as shown in Figure 1b. The electrode reaction device consisted of a magnesium alloy anode, an air cathode, and 250 mL of 3.5 wt.% NaCl electrolyte. Therein, a commercially available nickel grid combined with a MnO_2/C catalyst layer was used as the air cathode, with a naked area of 9 cm^2, and extruded specimens with 1 cm^2 exposed surface served as the metal anode. The LANDdt V7 3.0.1 software was employed to note the discharge data for current den-

sities of 5, 20, 40, and 80 mA cm^{-2} at 25 °C for 8 h. The Mg alloy anode's discharge specific capacity and anode efficiency were calculated during the discharge process with Equations (3) and (4), as follows [29,30]:

$$Discharge\ capacity(mAh \times g^{-1}) = \frac{I \times t \times A}{\Delta w} \quad (3)$$

$$Anode\ efficiency(\%) = \frac{3.6 \times I \times t \times A \times M}{2F \times \Delta w} \times 100\% \quad (4)$$

where I is the discharge current density (mA·cm^{-2}); t is the discharge time (h); A is the anode working surface area (cm^{-2}); ΔW is the mass loss before and after discharge (g); M is the molar mass (g·mol^{-1}); and F is the Faraday's constant (96,485 C·mol^{-1}).

3. Results and Discussion

3.1. Microstructure Analysis of Extruded Mg-8Li-xZn-yGd Alloys

Figure 2 shows the longitudinal optical microstructures of the extruded alloys. The light-colored α-Mg phase and the dark-colored β-Li phase were distributed alternately. The α-Mg grains are plastically deformed after extrusion deformation, the grains are elongated along the extrusion direction under the influence of extrusion pressure, and the second phase is broken during the extrusion procedure. As shown in Figure 2b–d, the crushed second phase is distributed parallel to the extrusion direction, forming extrusion streamlines to some extent. With the increasing Zn/Gd ratio, the extrusion streamlines formed by the fragmentation of the reticulated phase become more obvious and coarser. Figure 2a,c,e reveal that when the Zn/Gd ratio is 1, increasing the Zn and Gd element contents could refine the extrusion streamlines, enhancing the continuity of the crushed second phase. The light-colored matrix undergoes obvious refinement, indicating that increased Zn and Gd contents play an obvious role in graining refinement.

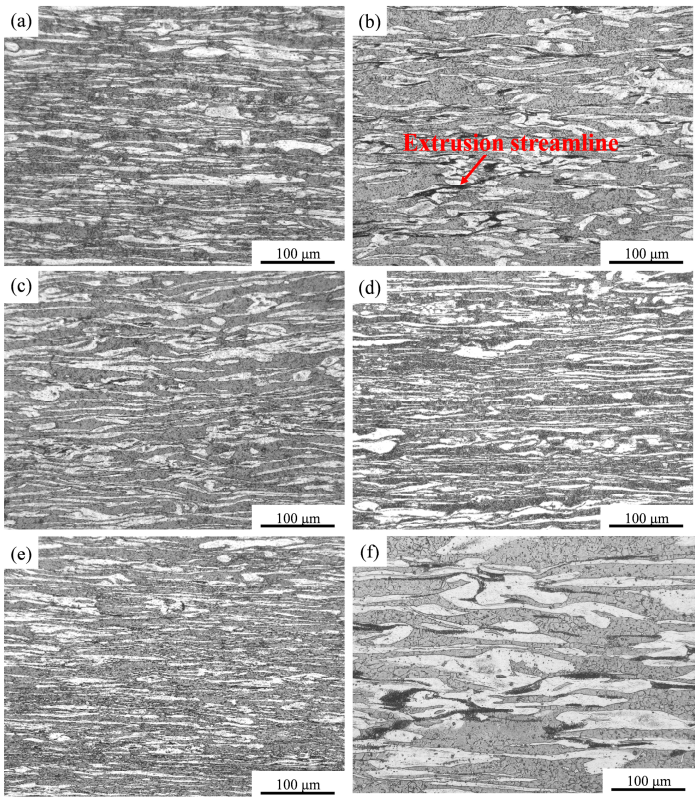

Figure 2. Optical microstructures of extruded Mg-8Li-xZn-yGd alloy: (**a**) LZG811; (**b**) LZG821; (**c**) LZG822; (**d**) LZG823; (**e**) LZG833; (**f**) large-sized LZG821.

Many fine equiaxed grains are able to be noticed inside the β-Li phase, indicating that dynamic recrystallization occurs during extrusion (Figure 2f), and a spot of equiaxed grains of larger sizes may be the result of grain growth after dynamic recrystallization [31–33].

The XRD phase analysis of the extruded Mg-8Li-xZn-yGd alloy is shown in Figure 3, and it can be inferred that the second phases in the extruded alloy are the W phase, the Mg_3Gd phase, and the LiMgZn phase. SEM image and EDS energy spectrum analyses of the extruded alloys are shown in Figure 4. The α-Mg and β-Li matrix phases are elongated along the extrusion direction. The eutectic reticulated W phase is broken, forming extrusion streamlines along the extrusion direction. It is shown that during the solidification process, Gd atoms are prone to precipitate at the grain boundaries, effectively retarding grain growth. Moreover, intermetallic compounds generated along the grain boundaries will hinder the further growth of grains, and this phenomenon will also lead to grain refinement [21].

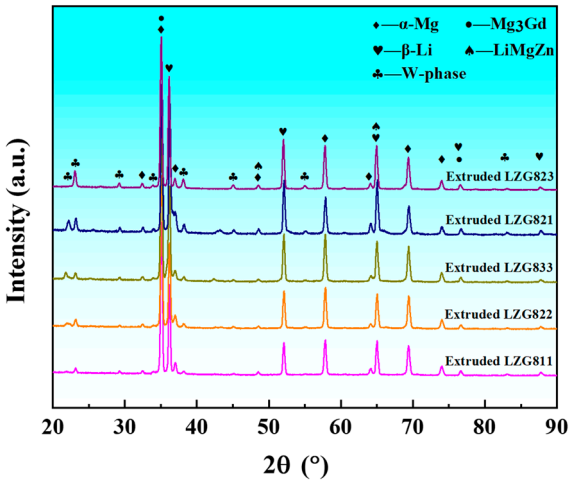

Figure 3. XRD patterns of extruded Mg-8Li-xZn-yGd alloys.

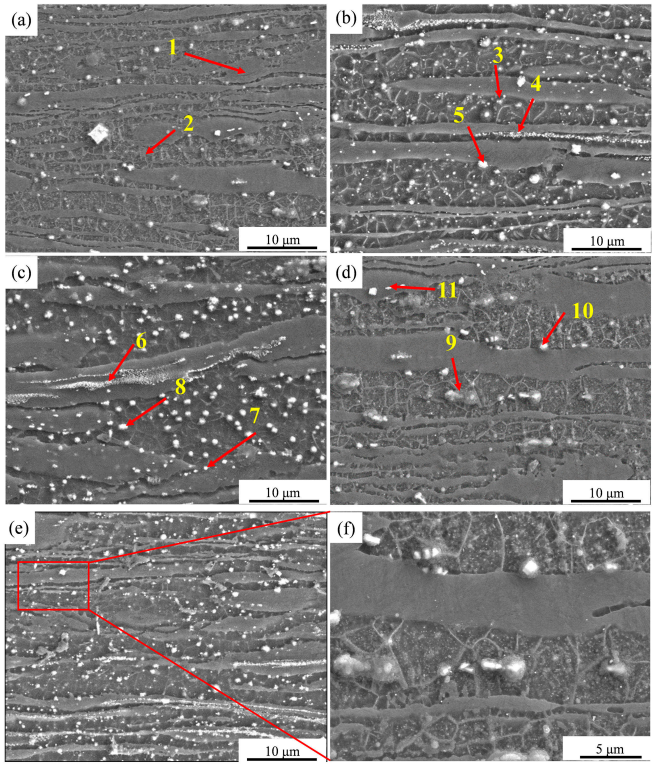

Figure 4. SEM microstructures of extruded Mg-8Li-xZn-yGd alloys: (**a**) LZG811; (**b**) LZG821; (**c**) LZG822; (**d**) LZG823; (**e**) LZG833; (**f**) locally magnified LZG833.

Figure 4f shows that dynamic recrystallization occurs during the process of extrusion. The alloy grain size decreases dramatically after extrusion, and the crushed W phase promotes the recrystallization through the particle-induced nucleation mechanism. The results of the EDS analysis of the marked positions in Figure 4 are presented in Table 3.

Table 3. EDS points analysis results of extruded Mg-8Li-xZn-yGd alloys.

Marking Point	Mg (at.%)	Zn (at.%)	Gd (at.%)	Second Phase
1	99.51	0.43	0.06	α-Mg
2	99.41	0.38	0.21	β-Li
3	99.27	0.73	\	MgLiZn
4	96.23	2.17	1.6	W phase ($Mg_3Zn_3Gd_2$)
5	72.72	0.56	26.72	Mg_3Gd
6	89.12	6.14	4.74	W phase ($Mg_3Zn_3Gd_2$)
7	98.72	1.26	0.02	MgLiZn
8	76.46	1.14	22.41	Mg_3Gd
9	98.28	1.72	\	MgLiZn
10	80.04	0.64	19.32	Mg_3Gd
11	87.43	8.61	3.96	W phase ($Mg_3Zn_3Gd_2$)

Through alloying elements analysis of the marked points, it can be found that the three elements of Mg, Zn, and Gd appear simultaneously at points 4, 6, and 11, and the Zn to Gd ratio is approximately 1.5. It can be determined that these granules are the W phase after being crushed during the extrusion process, which agrees with the XRD detection results. The points 5, 8, and 10 are mainly dominated by the Mg and Gd elements, in which the content of Gd is close to 25 at.%; it is believed that these particles are massive Mg_3Gd phases. Points 3, 7, and 9 only consist of the Mg and Li elements (with a small amount of Gd at point 7), and the light Li elements cannot be detected through EDS detection. Combined with the XRD results, it is presumed that the granular phase at this site is the MgLiZn phase. Points 1 and 2 are the α-Mg and β-Li phases, respectively, and varying amounts of other elements have been found in the EDS, which is mainly due to small amounts of Zn and Gd elements solidly dissolved within the matrix.

Figure 5 shows the EDS elemental distribution mapping of the extruded Mg-8Li-2Zn-2Gd alloy. It shows that the Mg element is mainly distributed in the matrix, while the Zn and Gd elements mainly appear in the extrusion streamline. It is also clear that the Zn element is more inclined to be solidly soluble in the β-Li matrix, while the Gd element is more solidly soluble in the α-Mg matrix.

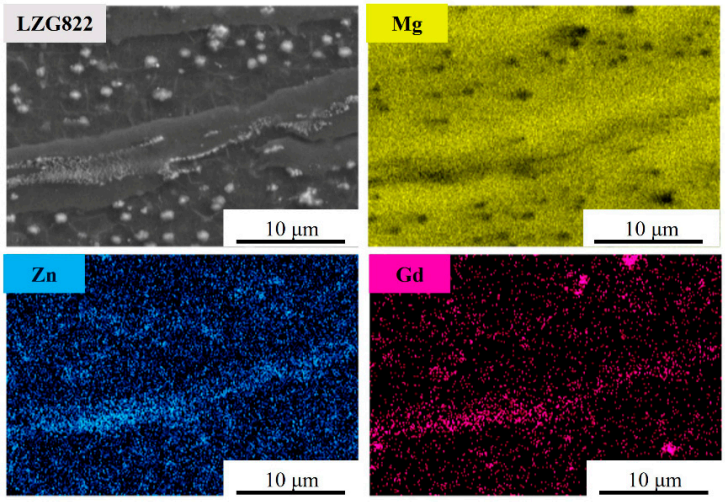

Figure 5. EDS elemental distribution mapping of extruded LZG822 alloy.

3.2. Corrosion Resistance of Extruded Mg-8Li-xZn-yGd Mg-Air Anode Alloys

3.2.1. Analysis of Static Corrosion Behavior

Figure 6 demonstrates the weight loss corrosion rate of Mg-8Li-xZn-yGd alloys in 3.5 wt.% NaCl solution. As shown here, the corrosion rate decreases gradually with an increasing Zn/Gd ratio, and the extruded LZG821 alloy shows the optimal corrosion resistance, with a corrosion rate of only 4.93 mm·year^{-1}. When the Zn/Gd ratio is 1, the corrosion rate is also decreased by the addition of further Zn and Gd elements.

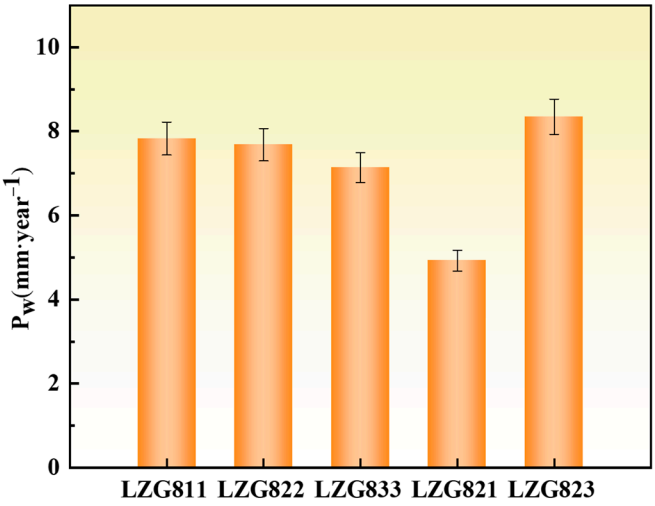

Figure 6. Weight loss corrosion rates of Mg-8Li-xZn-yGd alloys after 24 h immersion in 3.5 wt.% NaCl solution.

3.2.2. Analysis of Electrochemical Corrosion Behavior

The OCP curves of the extruded Mg-8Li-xZn-yGd alloys are shown in Figure 7. They reveal that the steady-state open circuit potential is reached after 700 s, and the extruded LZG833 and LZG821 alloys exhibit relatively higher potentials. When the corrosion proceeds to the middle stage, the extruded LZG822, LZG833, and LZG821 alloys show large fluctuations, demonstrating that the corrosion product layer of the alloys is unstable at this stage. Once the product film falls off, the open circuit potential will move rapidly in a negative direction.

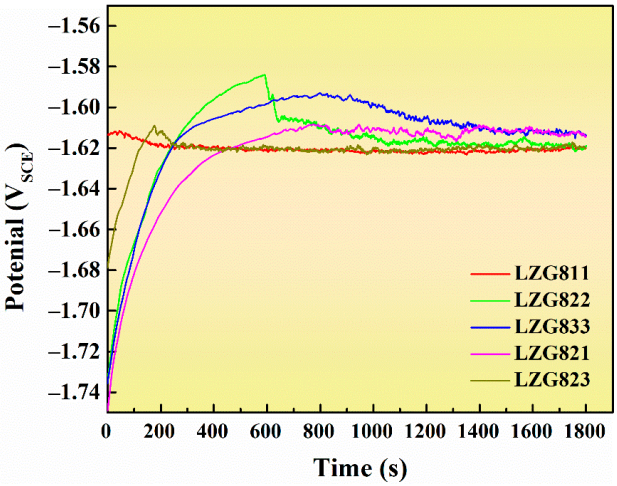

Figure 7. Open circuit potential curves of extruded Mg-8Li-xZn-yGd alloys.

The LZG822 alloy shows a higher peak value and a rapid decrease, which is due to the adsorption of Cl− on the oxide film surface and the 'cathode activation', with the ($2H_2O + 2e^- = 2OH^- + H_2$) reaction's appearance on a mass of cathode second phases, causing

local corrosion. The extruded LZG811 and LZG823 alloys are suitable for use as anode alloys for Mg-air batteries, due to the short time it takes for their open circuit potential to stabilize and their minuscule potential amplitude.

Table 4 shows the steady-state OCP values of the extruded Mg-8Li-xZn-yGd alloys. The OCP values of the experimental alloys increase with the increased Zn/Gd ratio, indicating that the coarsening of the W phase could slow down the self-corrosion tendency. When the Zn/Gd ratio is 1, the LZG811 alloy shows a more negative OCP value, and the difference among the three alloys is not much. This means that the OCP value of the LZG833 alloy at a non-load state is higher, and the electrochemical activity is also higher, indicating that this alloy will provide higher discharge voltage when it is used as a Mg-air battery anode material.

Table 4. Steady-state OCP values of Mg-8Li-xZn-yGd alloys after 700 s.

Alloy	LZG811	LZG822	LZG833	LZG821	LZG823
OCP/V	−1.62051 ± 0.017	−1.61893 ± 0.009	−1.61244 ± 0.018	−1.61234 ± 0.012	−1.62068 ± 0.024

Figure 8 shows the PDP curves of the extruded Mg-8Li-xZn-yGd alloys in 3.5 wt.% NaCl solution. Relevant fitting self-corrosion potentials (E_{corr}) and self-corrosion current densities (I_{corr}), obtained by Tafel extrapolation, are listed in Table 5. As shown in Figure 8, the extruded alloys show extensive Tafel zones at the cathodic branch, demonstrating stable hydrogen evolution reactions. The E_{corr} of each alloy adheres to the following pattern: LZG821 (−1.522 V) > LZG822 (−1.566 V) > LZG833 (−1.575 V) > LZG811 (−1.595 V) > LZG823 (−1.623 V). These results indicate that the LZG823 alloy exhibits the highest level of electrochemical activity. For Mg-air battery anode alloys, the electrochemical activity is considered first, but the anode efficiency is also of great concern [34]. Reducing the self-corrosion rate is one of the ways to improve the anode efficiency of anode alloys. The I_{corr} of each sample, measured by Tafel extrapolation, adheres to the following pattern: LZG821 < LZG833 < LZG822 < LZG811 < LZG823. As the Zn/Gd ratio increases, the alloy's I_{corr} decreases, but the corrosion resistance increases. The extruded LZG821 alloy has the lowest I_{corr} and the strongest corrosion resistance, with an average corrosion rate, P_i, of 0.439 mm·year^{-1}. When the Zn/Gd ratio is 1, by increasing the elemental contents of Zn and Gd, the quantity of W phases increases, and the corrosion resistance is enhanced. The lowest corrosion rate is observed in the extruded LZG833 alloy, with a P_i of 0.611 mm·year^{-1}.

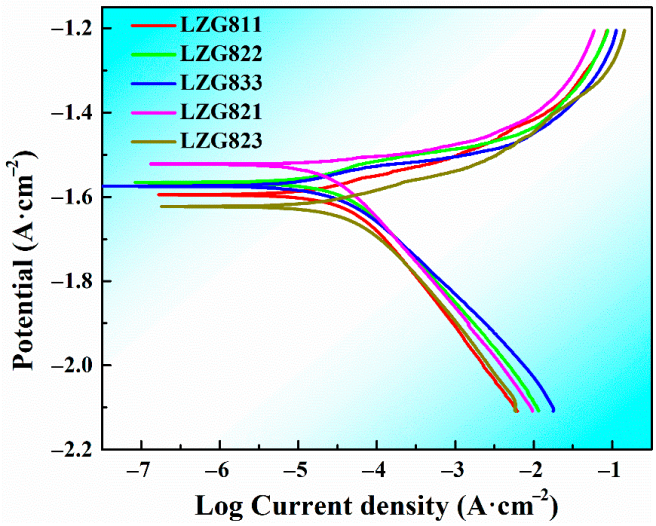

Figure 8. PDP curves of extruded Mg-8Li-xZn-yGd alloys.

Table 5. PDP curve fitting results of Mg-8Li-xZn-yGd alloys.

Alloys	E_{corr}/V	I_{corr}/mA·cm^{-2}	P_i/mm·year^{-1}
LZG811	−1.595	0.03296	0.753
LZG822	−1.566	0.02964	0.677
LZG833	−1.575	0.02672	0.611
LZG821	−1.522	0.01922	0.439
LZG823	−1.623	0.03655	0.835

The electrochemical impedance manifestation of the extruded Mg-8Li-xZn-yGd alloys in 3.5 wt.% NaCl solution is displayed in Figure 9. Figure 9a represents the Nyquist curves of the extruded alloys, from which it can be observed that there is one high-frequency capacitive arc, one mid-frequency capacitive arc, and one low-frequency inductive arc for all five extruded alloys. It indicates that the extruded alloys with different compositions have the same corrosion mechanism. The capacitive arc radius (R_p) in the high-frequency region increases as the Zn/Gd ratio increases. A higher R_p represents better corrosion resistance [35,36]. The extruded LZG821 alloy has the largest capacitance arc radius, indicating that this alloy has the largest charge transfer resistance, and the high resistance hinders the corrosion of the α-Mg substrate, thus causing a lower corrosion rate [37–39]. The LZG823 alloy, with the smallest Zn/Gd ratio, has the smallest low-frequency inductive arc radius, which indicates that this alloy has a strong corrosion product film precipitation ability and exhibits strong discharge activity when used as a Mg-air battery anode material [40,41]. Figure 9b shows the bode phase angle versus impedance modulus plots for different alloys in descending order of impedance modulus: LZG821 > LZG833 > LZG822 > LZG811 > LZG823. The corrosion product layer of the extruded LZG821 alloy has a better protection effect against alloy corrosion, which agrees with the results presented by the Nyquist curves.

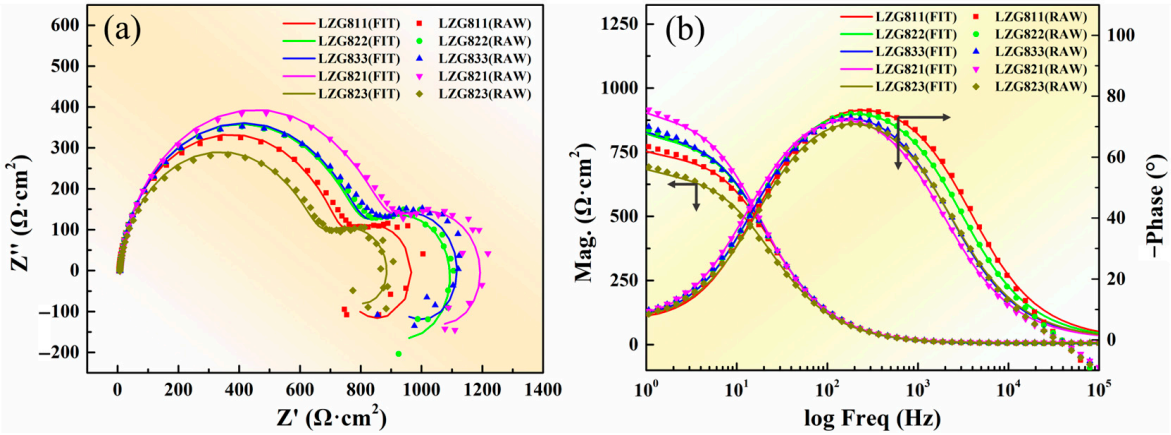

Figure 9. Electrochemical impedance spectra (EIS) of extruded Mg-8Li-xZn-yGd alloys: (**a**) Nyquist curves; (**b**) bode phase angle plots and impedance mode plots.

Figure 10 shows the EIS equivalent circuit, which is consistent for the five extruded alloys due to the same reaction mechanism. The equivalent circuit of the extruded alloys consists of the solution resistance R_s, the double electric layer capacitance CPE_{dl}, the charge transfer resistance R_{ct}, the corrosion product layer capacitance CPE_f, and the surface oxidized layer resistance R_f, as well as the inductance L and resistance R_L. CPE_{dl} and R_{ct} are connected in parallel to simulate the process of contacting the alloy surface with the electrolyte, CPE_f and R_f are connected in parallel to represent the influence of the corrosion product layer on the alloy corrosion property, and the inductance L and R_L are used in series to represent the rupture stage of the oxide product layer. The extruded LZG811 and LZG823 alloys have a finer and more uniform grain size, and their oxide film shedding rate is slow, so the mid-frequency capacitive arc appeared in these extruded alloys.

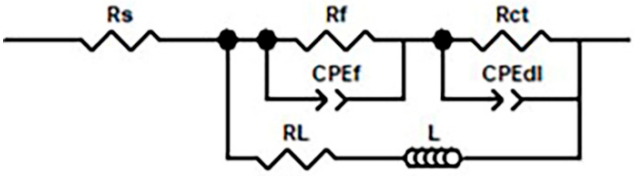

Figure 10. EIS equivalent circuit of extruded Mg-8Li-xZn-yGd alloys.

The related fitting parameters of the equivalent circuit are shown in Table 6. The values of charge transfer resistance R_{ct} and oxide layer resistance R_f increase with increases in the Zn/Gd ratio, indicating that the micro-galvanic corrosion is weakened; a dense and stable corrosion product layer plays an essential role during the corrosion process. When the Zn/Gd ratio is 1, the corrosion resistance of the fitted circuit is improved by increasing the Zn and Gd elemental contents. The extruded LZG821 alloy exhibits the best corrosion resistance and the LZG823 alloy has the optimal electrochemical activity, which is the same conclusion as was reached after the static corrosion experiments.

Table 6. Impedance spectrum fitting results of extruded Mg-8Li-xZn-yGd alloys.

Alloys	R_S	CPE_{dl}		R_{ct}	CPE_f		R_f	L	R_L
	$\Omega \cdot cm^2$	Y_1/ $\mu\Omega^{-1} \cdot cm^{-2} \cdot S^n$	n_1	$\Omega \cdot cm^2$	Y_2/ $\mu\Omega^{-1} \cdot cm^{-2} \cdot S^n$	n_2	$\Omega \cdot cm^2$	$H \cdot cm^2$	$\Omega \cdot cm^2$
LZG811	4.45	18.08	0.937	719.4	33.13	0.802	342.4	25,864	2417
LZG822	5.63	19.02	0.931	778.6	26.86	0.791	379.6	52,325	2275
LZG833	7.58	19.20	0.930	783.2	28.92	0.762	474.5	34,885	2895
LZG821	8.66	20.13	0.925	860.9	28.11	0.78	411.4	63,879	3460
LZG823	7.10	22.16	0.918	642.8	32.39	0.775	290.7	52,189	3172

3.3. Discharge Properties of Extruded Mg-8Li-xZn-yGd Mg-Air Anode Alloys

3.3.1. Constant Current Discharge Performance Analysis

The extruded Mg-8Li-xZn-yGd Mg-air anode alloys' discharge curves in 3.5 wt.% NaCl solution are revealed in Figure 11. At low current densities ($\leq$20 mA·cm^{-2}), the alloy discharge voltage is high, and the discharge trend is also relatively stable. At a 5 mA·cm^{-2} current density, the discharge voltage is at its most stable, indicating that the alloy has the most stable corrosion product generation and shedding rate. Compared with cast Mg-8Li-xZn-yGd anode alloys, the extruded alloys show superior discharge characteristics. The extruded alloy has more grain boundaries exposed in the electrolyte that can act as reaction channels with increased discharge time, which increases the area of discharge reaction and makes the alloy exhibit higher amounts of energy to preferentially dissolve, thus promoting the improvement of its discharge performance [42–44]. By increasing the current density, the influence of corrosion products on the discharge voltage is increased. The precipitation and dissolution ability of the corrosion product layer determines the development of the alloy's discharge behavior. Consequently, the LZG821 alloy, with the strongest corrosion resistance, is affected by its insufficient ability to decompose corrosion products, and its discharge voltage is the lowest.

Under high current densities ($\geq$40 mA·cm^{-2}), the discharge voltage shows large fluctuations in all anode alloys, which is attributed to the corrosion products' sudden detachment from each anode alloy's surface. It also results in the exposure of new Mg alloy substrate to the electrolyte, and the sudden increase in the working area of the discharge improves the operating voltage. Since the stability of the corrosion product layer varies for alloys with different compositions, the precipitation and dissolution ability of the product layer is inconsistent, leading to unstable discharge voltage [45]. Upon increasing the current density to 80 mA·cm^{-2}, dense oxidation products make the discharge voltage and discharge duration highly contingent, which is not suitable for many applications.

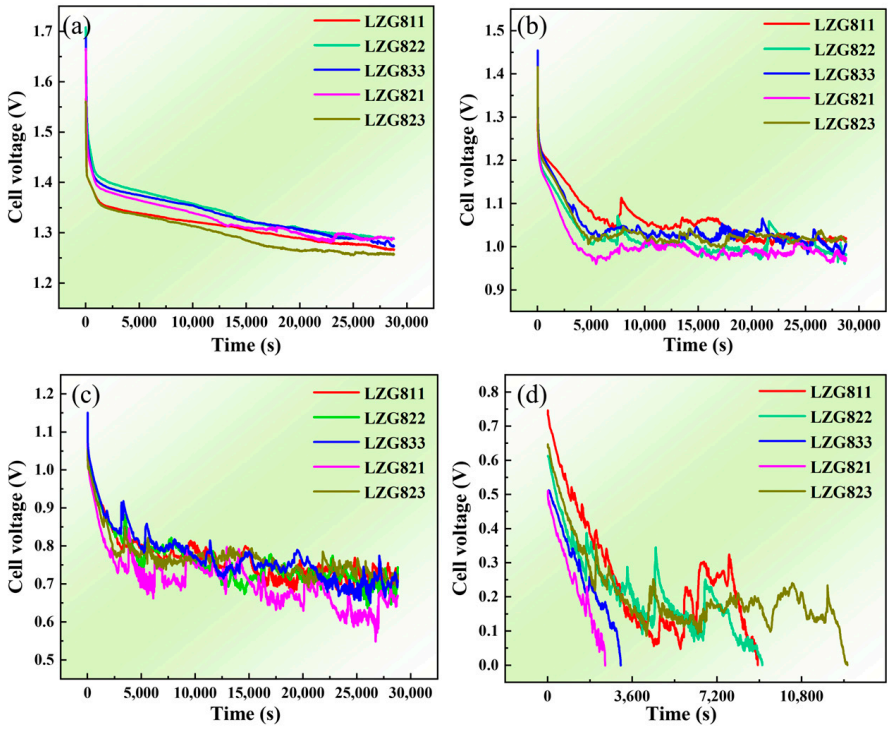

Figure 11. Constant current discharge curves of extruded Mg-8Li-xZn-yGd alloys at different current densities: (**a**) 5 mA·cm^{-2}; (**b**) 20 mA·cm^{-2}; (**c**) 40 mA·cm^{-2}; (**d**) 80 mA·cm^{-2}.

Figure 12 shows the discharge characteristic curves of the extruded Mg-8Li-xZn-yGd alloys. The specific data are summarized in Table 7. The discharge properties of different alloys are significantly reduced, which is consistent with the phenomenon reflected by the discharge voltage. The grain boundary density increases as the grain size decreases. High grain boundary density improves the discharge activity of the anode alloys, and intergranular corrosion has a limited effect on the experimental alloys.

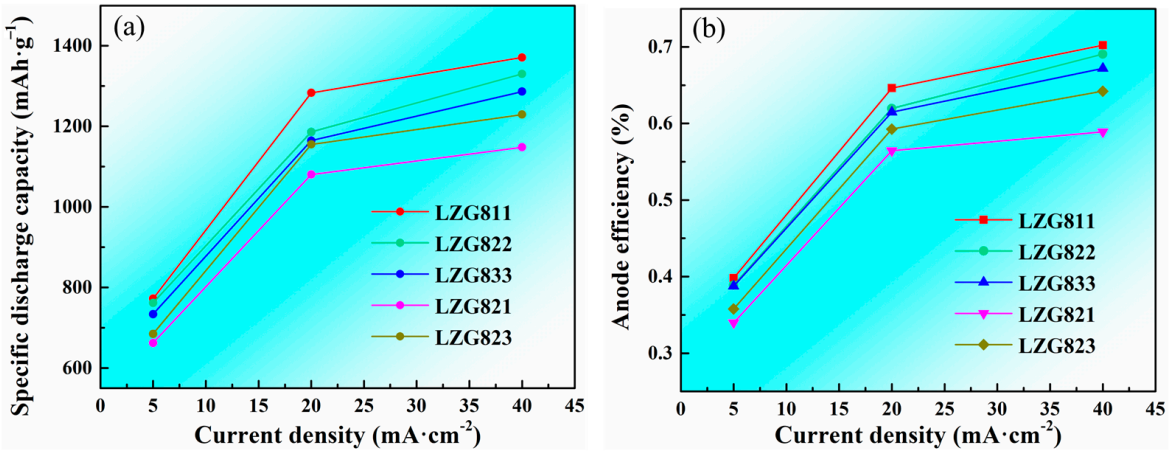

Figure 12. Discharge characteristics of extruded Mg-8Li-xZn-yGd alloys in 3.5 wt.% NaCl solution: (**a**) specific discharge capacity; (**b**) anode efficiency.

When the Zn/Gd ratio is 1, the specific discharge capacity and anode efficiency decrease with increases in the Zn and Gd element contents. The extruded LZG811 alloy maintains the highest discharge performance, with a specific discharge capacity of 1371.04 mA·g^{-1} at a current density of 40 mA·cm^{-2}, and its anode efficiency reaches nearly 70%. Although the extruded LZG823 alloy is the most electrochemically active, its high self-corrosion efficiency results in significant mass loss. The extruded LZG821 alloy is

affected by the densification of the product layer and has a lower specific discharge capacity as well as a low anode efficiency, which are 1148.19 mA·g^{-1} and 59% at a current density of 40 mA·cm^{-2}.

Table 7. Discharge properties of extruded Mg-8Li-xZn-yGd alloys.

Alloys	Discharge Specific Capacity/mA·g^{-1}			Anode Efficiency/%		
	5 mA·cm^{-2}	20 mA·cm^{-2}	40 mA·cm^{-2}	5 mA·cm^{-2}	20 mA·cm^{-2}	40 mA·cm^{-2}
LZG811	772.20	1283.08	1371.04	40	65	70
LZG822	761.90	1186.06	1330.01	39	62	69
LZG833	733.95	1164.48	1286.17	39	62	67
LZG821	662.25	1080.35	1148.19	34	56	59
LZG823	684.93	1155.24	1229.35	36	59	64

Chen et al. [46] prepared a cast Mg-8Al-0.5Zn alloy and investigated the effect of outfield treatment on its anodic discharge performance, and the anode efficiency of the external field-treated Mg-8Al-0.5Zn anode alloy was about 63.3% at a current density of 40 mA·cm^{-2}. In comparison, the anode efficiency of the extruded LZG811 anode alloy prepared in this study reaches nearly 70% at a current density of 40 mA·cm^{-2}. Meanwhile, Mg-Li alloys are less dense and lighter in weight than other alloys, and their application range would be broader.

3.3.2. Surface Morphology of Extruded Alloys after Discharge

Figure 13 shows the SEM microstructures of the extruded Mg-8Li-xZn-yGd alloys after discharge at a 20 mA·cm^{-2} current density for 8 h. As can be seen, the corrosion pits of the extruded LZG811 alloy are uniform and shallow, indicating an excellent discharge performance.

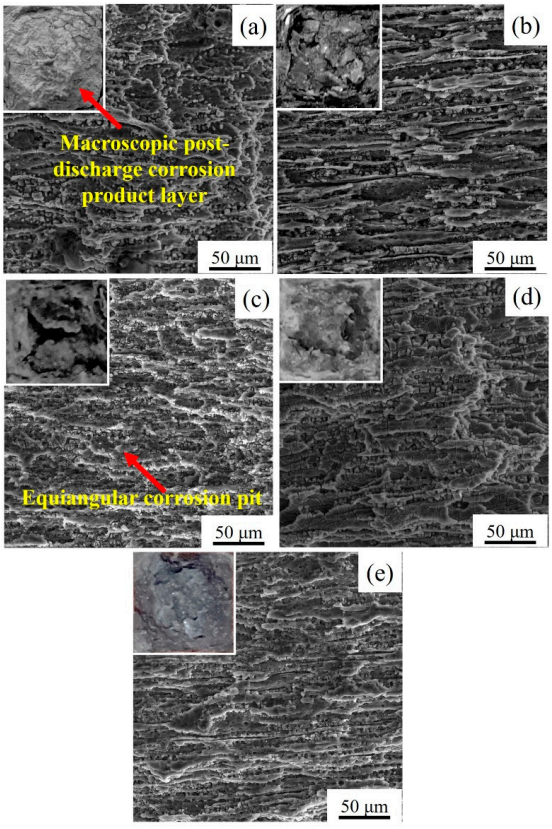

Figure 13. SEM microstructures of as-extruded Mg-8Li-xZn-yGd alloys after being discharged for 8 h at current density of 20 mA·cm^{-2}: (**a**) LZG811; (**b**) LZG821; (**c**) LZG822; (**d**) LZG823; (**e**) LZG833.

The corrosion pits of the alloy are significantly reduced after extrusion deformation, which is because the W phase is dispersed at the grain boundaries after extrusion crushing. The fine dispersed second phase particles are favorable for the formation of a continuous product film, which can be used as a physical barrier to impede corrosion diffusion, thus improving the corrosion resistance. Grain refinement also has an important impact on corrosion resistance. Grain refinement of the large pit may result in small equiangular pits, and these equiangular pits and grain boundaries can be used as physical barriers to inhibit the spread of corrosion. And smaller grain size is conducive to the formation of a continuous protective corrosion product film, reducing the surface film's cracking and effectively slowing down the self-corrosion of the alloy, thus improving the discharge performance.

4. Conclusions

The electrochemical performance and discharge behavior of extruded Mg-8Li-xZn-yGd alloys with an α-Mg and β-Li-based anode material are investigated by adjusting their Zn and Gd element contents and Zn/Gd ratio. The main purpose of this work is to investigate the discharge performance of ultralight α-Mg and β-Li-based Mg-8Li-xZn-yGd anode materials with different Zn/Gd ratios during constant current discharge tests of Mg-air batteries, and further, to analyze the effects of different compositions and microstructures on the negative difference effect, anodic dissolution reaction, and passive film. The following conclusions are summarized through the analysis of microstructure, corrosion, and discharge performance:

(1) The microstructures of the experimental alloys are composed of an α-Mg and β-Li dual matrix, with W-$Mg_3Gd_2Zn_3$, Mg_3Gd, and MgLiZn second phases. The second phases show no change compared with the cast condition. Meanwhile, extrusion deformation promotes the recrystallization process through the particle-induced nucleation mechanism. When the Zn/Gd ratio is 1, the W-$Mg_3Gd_2Zn_3$ phase content is increased by the further addition of Zn and Gd.

(2) The corrosion resistance is improved with an increasing Zn/Gd ratio, and the extruded Mg-8Li-2Zn-1Gd (LZG821) alloy has the optimum corrosion resistance, with a corrosion rate of 0.493 mm·year^{-1}, while the extruded LZG823 alloy has the best electrochemical activity. Dynamic recrystallization occurs during extrusion deformation, to reduce the effective corrosion area, improve the density of corrosion products, and enhance the corrosion resistance property.

(3) The electrical properties of the extruded Mg-8Li-2Zn-1Gd (LZG821) and Mg-8Li-2Zn-3Gd (LZG823) alloys decrease at high current densities. The extruded Mg-8Li-1Zn-1Gd (LZG811) alloy has the optimal discharge performance, with a discharge specific capacity of 1371.04 mA·g^{-1} at a current density of 40 mA·cm^{-2}, and the anode efficiency reaches nearly 70%.

Author Contributions: S.Y.: conceptualization, methodology, formal analysis, investigation, writing—original draft, funding acquisition. G.Z.: investigation, data curation, writing—review and editing, funding acquisition, supervision. Z.L., N.W. and H.H.: investigation, writing—review and editing, data curation. R.G.: writing—review and editing, project administration, funding acquisition, supervision. All authors have read and agreed to the published version of the manuscript.

Funding: This research was funded by the National Key Research and Development Program of China [grant no. 2022YFE0137900], the National Natural Science Foundation of China [grant no. 52305341], the Basic Scientific Research Project of Liaoning Provincial Education Department [JYTQN2023003, JYTMS20230031], and the National Natural Science Foundation of Liaoning Province [grant no. 2022-BS-261, 2022-BS-262].

Data Availability Statement: The raw data supporting the conclusions of this article will be made available by the authors on request.

Conflicts of Interest: The authors declare no conflicts of interest.

References

1. Li, Q.; Xiong, W.; Yu, S.; Liu, Y.; Li, J.; Liu, L.; Bi, X.; Zhu, G.; Liu, E.; Zhao, Y.; et al. Effect of Gd content on the discharge and electrochemical behaviors of the magnesium alloy AZ31 as an anode for Mg-air battery. *J. Mater. Sci.* **2021**, *56*, 12789–12802. [CrossRef]
2. Chu, S.; Majumdar, A. Opportunities and challenges for a sustainable energy future. *Nature* **2012**, *488*, 294–303. [CrossRef] [PubMed]
3. Fu, Y.H.; Zhao, H.; Piao, S.; Peaucelle, M.; Peng, S.; Zhou, G.; Ciais, P.; Huang, M.; Menzel, A.; Peñuelas, J.; et al. Declining global warming effects on the phenology of spring leaf unfolding. *Nature* **2015**, *526*, 104–107. [CrossRef] [PubMed]
4. Schmuch, R.; Wagner, R.; Hörpel, G.; Placke, T.; Winter, M. Performance and cost of materials for lithium-based rechargeable automotive batteries. *Nat. Energy* **2018**, *3*, 267–278. [CrossRef]
5. Zhang, X.; Wang, X.G.; Xie, Z.; Zhou, Z. Recent progress in rechargeable alkali metal-air batteries. *Green Energy Environ.* **2016**, *01*, 4–17. [CrossRef]
6. Taniguchi, A.; Fujioka, N.; Ikoma, M.; Ohta, A. Development of nickel/metal-hydride batteries for EVs and HEVs. *J. Power Sources* **2001**, *100*, 117–124. [CrossRef]
7. Durmus, Y.E.; Zhang, H.; Baakes, F.; Desmaizieres, G.; Hayun, H.; Yang, L.; Kolek, M.; Küpers, V.; Janek, J.; Mandler, D.; et al. Side by side battery technologies with lithium-ion based batteries. *Adv. Energy Mater.* **2020**, *10*, 89–110. [CrossRef]
8. Lee, J.S.; Kim, S.T.; Cao, R.; Choi, N.S.; Liu, M.; Lee, K.T.; Cho, J. Metal–air batteries with high energy density: Li-air versus Zn-air. *Adv. Energy Mater.* **2011**, *1*, 34–50. [CrossRef]
9. Li, Y.; Zhang, X.; Li, H.B.; Yoo, H.D.; Chi, X.; An, Q.; Liu, J.; Yu, M.; Wang, W.; Yao, Y. Mixed-phase mullite electrocatalyst for pH-neutral oxygen reduction in magnesium-air batteries. *Nano Energy* **2016**, *27*, 8–16. [CrossRef]
10. Tian, G.; Wang, J.; Xue, C.; Yang, X.; Wang, S.; Su, H. Ultra-light Mg–Li alloy by design to achieve unprecedented high stiffness using the CALPHAD approach. *Calphad* **2023**, *81*, 102556. [CrossRef]
11. Hirsch, J.; Al-Samman, T. Superior light metals by texture engineering: Optimized aluminum and magnesium alloys for automotive applications. *Acta Mater.* **2013**, *61*, 818–843. [CrossRef]
12. Zou, Y.; Zhang, L.; Wang, H.; Tong, X.; Zhang, M.; Zhang, Z. Texture evolution and their effects on the mechanical properties of duplex Mg-Li alloy. *J. Alloys Compd.* **2016**, *669*, 72–78. [CrossRef]
13. Ding, Z.Y.; Cui, L.Y.; Chen, X.B.; Zeng, R.C.; Guan, S.K.; Li, S.Q.; Zhang, F.; Zou, Y.H.; Liu, Q.Y. In vitro corrosion of micro-arc oxidation coating on Mg-1Li-1Ca alloy-The influence of intermetallic compound Mg2Ca. *J. Alloys Compd.* **2018**, *764*, 250–260. [CrossRef]
14. Liu, W.; Feng, S.; Li, A.; Zhao, J.; Wu, G.; Wang, X.; Xiao, L.; Ding, W. Effect of rolling strain on microstructure and tensile properties of dual-phase Mg–8Li–3Al–2Zn–0.5Y alloy. *J. Mater. Sci. Technol.* **2018**, *34*, 2256–2262. [CrossRef]
15. Chen, X.B.; Li, C.; Xu, D. Biodegradation of Mg-14Li alloy in simulated body fluid: A proof-of-concept study. *Bioact. Mater.* **2017**, *3*, 110–117. [CrossRef]
16. Zeng, R.C.; Sun, L.; Zheng, Y.F.; Cui, H.Z.; Han, E.H. Corrosion and characterization of dual phase Mg-Li-Ca alloy in Hank's solution: The influence of microstructural features. *Corros. Sci.* **2014**, *79*, 69–82. [CrossRef]
17. Zhou, Y.; Bian, L.; Chen, G.; Wang, L.; Liang, W. Influence of Ca addition on microstructural evolution and mechanical properties of near-eutectic Mg-Li alloys by copper-mold suction casting. *J. Alloys Compd.* **2016**, *664*, 85–91. [CrossRef]
18. Jang, H.S.; Seol, D.; Lee, J. Modified embedded-atom method interatomic potentials for Mg–Al–Ca and Mg–Al–Zn ternary systems. *J. Magnes. Alloys* **2021**, *9*, 317–335. [CrossRef]
19. He, F.Y.; Hu, W.X.; Liu, L.J.; Ma, S.B.; He, W. Effect of Zn addition on microstructure and mechanical properties of Mg-3Y-2Nd-0.5Zr alloy. *China Foundry* **2023**, *20*, 299–306. [CrossRef]
20. Gong, Y.; Wei, K.; Jiang, W.; Xiang, C.; Ding, H.; Wang, Z. Effect of Zn Addition on the Microstructure and Discharge Performance of Mg-Al-Mn-Ca Alloys for Magnesium-Air Batteries. *Metals* **2024**, *14*, 1014. [CrossRef]
21. Gong, C.; He, X.; Fang, D.; Liu, B.; Yan, X. Effect of second phases on discharge properties and corrosion behaviors of the Mg-Ca-Zn anodes for primary Mg-air batteries. *J. Alloys Compd.* **2020**, *861*, 158493. [CrossRef]
22. Wei, Z.; Zhang, J.; Bao, R.; Wu, R.; Zhang, H. Achieving high strength in a Mg–Li–Zn–Y alloy by α-Mg precipitation. *Mater. Sci. Eng. A* **2022**, *846*, 143272. [CrossRef]
23. Okafor, C.; Datye, A.; Zhang, S.; Schwarz, U.D.; Cai, Y.; Munroe, N. Development and biomaterial characterization of Mg-Li-Zn-Ca alloys. *Mater. Today Commun.* **2022**, *33*, 104999. [CrossRef]
24. Wang, J.; Xu, L.; Wu, R.; An, D.; Wei, Z.; Wang, J.; Feng, J.; Zhang, J.; Hou, L.; Liu, M. Simultaneous achievement of high electromagnetic shielding effectiveness (X-band) and strength in Mg-Li-Zn-Gd/MWCNTs composite. *J. Alloys Compd.* **2021**, *882*, 160524. [CrossRef]
25. Yin, S.; Duan, W.; Liu, W.; Wu, L.; Bao, J.; Yu, J.; Li, L.; Zhao, Z.; Cui, J.; Zhang, Z. Improving the corrosion resistance of MgZn1.2GdxZr0.18 (x=0, 0.8, 1.4, 2.0) alloys via Gd additions. *Corros. Sci.* **2020**, *177*, 108962. [CrossRef]
26. Sivashanmugam, A.; Renganathan, N.G.; Gopukumar, S. Performance of a magnesium-lithium alloy as an anode for magnesium batteries. *J. Appl. Electrochem.* **2004**, *34*, 1135–1139. [CrossRef]
27. Liu, X.; Liu, S.; Xue, J. Discharge performance of the magnesium anodes with different phase constitutions for Mg-air batteries. *J. Power Sources* **2018**, *396*, 667–674. [CrossRef]

28. *ASTM G31-21*; Standard Guide for Laboratory Immersion Corrosion Testing of Metals. ASTM International: West Conshohocken, PA, USA, 2012; pp. 1–9.
29. Moghanni-Bavil-Olyaei, H.; Arjomandi, J. Performance of Al-1Mg-1Zn-0.1Bi-0.02In as anode for the Al-AgO battery. *RSC Adv.* **2015**, *5*, 91273–91279. [CrossRef]
30. Liang, F.; Lu, H.; Jing, L.; Sun, Z. Performance of Al-0.6Mg-0.05Ga-0.1Sn-0.1In as anode for Al-air battery in KOH electrolytes. *J. Electrochem. Soc.* **2015**, *162*, A2623–A2627. [CrossRef]
31. Liu, Y.; Yuan, G.; Zhang, S.; Zhang, X.; Lu, C.; Ding, W. Effects of Zn/Gd ratio and content of Zn, Gd on phase constitutions of Mg alloys. *Mater. Trans.* **2008**, *49*, 941–944. [CrossRef]
32. Chang, T.C.; Wang, J.Y.; Chu, C.L.; Lee, S. Mechanical properties and microstructures of various Mg-Li alloys. *Mater. Lett.* **2006**, *60*, 3272–3276. [CrossRef]
33. Luo, Z.; Zhang, S.; Tang, Y.; Zhao, D. Quasicrystals in as-cast Mg-Zn-RE alloys. *Scr. Metall. Mater.* **1993**, *28*, 1513–1518. [CrossRef]
34. Wu, J.; Wang, R.; Feng, Y.; Peng, C. Effect of hot rolling on the microstructure and discharge properties of Mg-1.6 wt.% Hg-2 wt.% Ga alloy anodes. *J. Alloys Compd.* **2018**, *765*, 736–746. [CrossRef]
35. Xie, J.S.; Wang, L.L.; Zhang, J.H.; Lu, L.W.; Zhang, Z.; He, Y.Y.; Wu, R.Z. Developing new Mg alloy as potential bone repair material via constructing weak anode nano-lamellar structure. *J. Magnes. Alloys* **2023**, *11*, 154–175. [CrossRef]
36. Geng, X.; Dong, Q.; Zhang, X. Improved corrosion properties of Mg-Gd-Zn-Zr alloy by micro-arc oxidation. *Metals* **2024**, *14*, 236. [CrossRef]
37. Wan, D.Q.; Sun, Y.M.; Xue, Y.D.; Dong, S.Y.; Han, G.L.; Wang, Y.; Yang, F.; Tang, H.; Wang, Y.Y. Improvement in corrosion resistance of Mg97Zn1Y2 alloy by Zr addition. *China Foundry* **2024**. [CrossRef]
38. Geng, X.; Jiang, J.; Zhang, X. Corrosion Behavior of Mg-xGd-1Zn-0.4Zr Alloys with Different Gd Additions for Biomedical Application. *Metals* **2022**, *12*, 1763. [CrossRef]
39. Zhang, J.; Li, M.; Lai, Y.; Wen, L.; Ai, Y.; Ren, X.; Zhang, W. Study on the Microstructure and Properties of Mg-Gd-Ni-Y Alloy Containing LPSO Phase. *Metals* **2023**, *13*, 1989. [CrossRef]
40. Wan, D.Q.; Xue, Y.D.; Hu, J.J.; Wang, H.B.; Hou, W. Corrosion and chemical behavior of Mg97Zn1Y2-1wt.%SiC under different corrosion solutions. *China Foundry* **2021**, *18*, 68–74. [CrossRef]
41. Bian, J.C.; Yu, B.Y.; Hao, J.F.; Zhu, H.W.; Wu, H.S.; Chen, B.; Li, W.R.; Li, Y.F.; Zheng, L.; Li, R.X. Improvement of microstructure, mechanical properties, and corrosion resistance of WE43 alloy by squeeze casting. *China Foundry* **2022**, *19*, 419–426. [CrossRef]
42. Wang, N.; Li, W.; Huang, Y.; Wu, G.; Hu, M.; Li, G.; Shi, Z. Wrought Mg-Al-Pb-RE alloy strips as the anodes for Mg-air batteries. *J. Power Sources* **2019**, *436*, 226855. [CrossRef]
43. Wang, N.; Mu, Y.; Li, Q.; Shi, Z. Discharge and corrosion behaviour of AP65 magnesium anode plates with different rolling reductions. *RSC Adv.* **2017**, *7*, 53226–53235. [CrossRef]
44. Zhang, G.Z.; Wang, C.F.; Yin, S.Q.; Teng, D.; Guan, R.G. Development of low-carbon energy storage material: Electrochemical behavior and discharge properties of iron-bearing Al–Li-based alloys as Al–air battery anodes. *J. Power Sources* **2023**, *585*, 233654. [CrossRef]
45. Liu, X.; Zhang, P.J.; Xue, J.L. The role of micro-naoscale AlSb precipitates in improving the discharge performance of Al-Sb alloy anodes for Al-air batteries. *J. Power Sources* **2019**, *425*, 186–194. [CrossRef]
46. Chen, X.; Liao, Q.; Le, Q.; Zou, Q.; Wang, H.; Atrens, A. The influence of samarium (Sm) on the discharge and electrochemical behaviors of the magnesium alloy AZ80 as an anode for the Mg-air battery. *Electrochim. Acta* **2020**, *348*, 136315. [CrossRef]